Screen-printed flexible thermoelectric generator with directional heat collection design

Pin-Shiuan Chang , Chien-Neng Liao *

Department of Materials Science and Engineering, National Tsing Hua University, Hsinchu, 30013, Taiwan

ABSTRACT

A thermoelectric generator (TEG) was fabricated on a flexible substrate by screen printing and pressured sintering techniques for low-temperature heat harvesting applications. The screen-printed Bi-Sb-Te (p-type) and Bi-Se-Te (n-type) films that are sintered at 345 °C under a pressure of 25 MPa show the respective thermoelectric power factor of 14.3 and 8.4 μW/cm·K² at room temperature. A planar TEG made of three pairs of Bi-Sb-Te and Bi-Se-Te thermoelements delivers an output power of 50 μW at a temperature difference of 54.9 °C. The flexible TEG shows no electrical degradation after 1000 cycles of bending in the longitudinal and transverse directions of the thermoelements. A directional heat collection design is proposed to maximize the heat supply area of planar TEGs. The fabricated TEG can attain a maximum output power density of 58.3 μW/cm² under a temperature difference of 5.7 °C with a graphite heat transmission layer attached to a heat source at the temperature of 39.8 °C. It can serve as a self-sustained power source for wearable electronics and sensing devices by harvesting thermal energy from environment or human body.

© 2020 Elsevier B.V. All rights reserved.

1. Introduction

A thermoelectric generator (TEG) composed of paired p- and n-type thermoelements can convert heat into electricity under a temperature difference (ΔT) across the thermoelements [1]. The TEGs are generally divided into three categories: bulk, thick-film and thin-film (<10 μm) according to their thermoelement thickness. Generally, the TEG conversion efficiency depends on ΔT and figure-of-merit ($z = S^2\sigma/\kappa$, S: Seebeck coefficient, σ: electrical conductivity, κ: thermal conductivity) of the thermoelements. Extensive research efforts have been devoted to improving the figure-of-merit of thermoelectric materials employed in TEG applications, such as silicide [2], PbTe [3−5], half-Heusler [6] and perovskite-type compounds [7,8]. Additionally, the TEG output power also varies with the size and number of thermoelements in the thermoelectric module. To make a fair comparison of TEG performance, a thermoelectric efficiency factor ($\varphi = P_D/\Delta T^2$, P_D: output power density) has been proposed as a performance metrics for various TEGs with different structural configuration, operation conditions and heat sink/source design [9]. A thorough review on

the emerging trend and progresses of TEGs from 1989 to 2017 has revealed that nearly 86.2% of bulk TEGs and 44.1% of thick/thin film TEGs attained a φ value among 0.001 to 4 μWcm⁻²K⁻² [10]. It is worth mentioning that even though the film-type TEGs have lower efficiency factors than the bulk ones, the number of research works reported on the film-type TEGs is almost twice than that on the bulk TEGs due to the advantages of material saving and ease of fabrication [10].

The thermoelements in the film-type TEGs can be arranged with either a vertical or a planar configuration [11]. However, the vertical one can only establish a smaller ΔT and deliver lower output power due to the shorter thermoelement length. Moreover, metallic electrode/thermoelement junctions may contribute a large fraction of electrical and thermal resistance and lead to poor output performance for the vertical film-type TEGs [12]. On the other hand, the shortcoming of planar film-type TEGs is also obvious − a lower output power density due to a bigger device footprint. Nevertheless, the deficiency can be alleviated by stacking arrangement and improvement of thermoelement properties. A planar micro-radioisotope TEG with a 30-layer stacking configuration has demonstrated a volume power density of ~500 μW/cm³ at a temperature difference of 48 K [13].

The thermoelements in the film-type TEGs are frequently prepared by printing [14−16], sputtering [17−19], co-evaporation [20]

---

* Corresponding author.
  E-mail address: cnliao@mx.nthu.edu.tw (C.-N. Liao).

and chemical vapor deposition methods [21]. Especially, the printing technique has been massively employed in making thick-film TEGs owing to its process convenience and cost-saving advantages. Nevertheless, the printed films usually suffer poor electrical conductivity after thermal curing at elevated temperature, mainly due to the porosity or organic residues in the post-cured films [22,23]. Engineering of printing paste ingredients and sintering process conditions becomes essential for improving properties of printed thermoelements. A nano-solder approach has been employed to bridge the interfaces between the Bi-Sb-Te powders in the printed thermoelements by adding Te nano-particles in the printing paste [24]. The sintered Bi-Sb-Te film reveals an excellent power factor ($PF = S^2\sigma$) of 30 μW/cm·K^2 at room temperature. Generally, the electrical conductivity of the printed films can be improved by raising sintering temperature. Nevertheless, if the thermoelements are implemented on a flexible substrate, e.g. polyimide (PI), the thermal endurance of polymer substrate would prevent the elevation of process temperature beyond the glass transition point. It has been suggested that the printed thermoelectric films can be densified at a lower process temperature by applying mechanical pressure during thermal curing [22,23]. Some post-treatments may also be applied to improve the thermoelectric properties of thermoelectric films [25].

Besides improving thermoelement properties, the arrangement of heat sink/source is also essential for TEG applications. For planar film-type TEGs, the heat sink and source must be in good contact with the hot and cold sides of the TEG, respectively. Such an arrangement may not be suitable for an isothermal planar heat source that requires an appropriate heat conduction and isolation design. Moreover, the thermal contact resistance between the TEG and heat sink/source also needs further attention. An intimidate and full coverage of heat sink/source contact area is desired to reduce the thermal contact resistance for attaining the maximum ΔT across the thermoelements. Flexible film-type TEGs are highly preferred for non-planar heat sink/source and dynamically moving environment. The major progress of flexible thermoelectric materials and printing based TEGs can be found in some recent review articles [26–28]. In this study we have fabricated a flexible planar TEG using screen printing and pressured sintering techniques. The transport properties of the screen-printed Bi-Sb-Te and Bi-Se-Te films on a flexible PI substrate were reported. The output performance and flexibility of the planar TEG were measured and evaluated. A directional heat collection design to distribute heat from a planar source to a planar TEG is also presented.

2. Experimental details

Bi-Sb-Te (p-type) and Bi-Se-Te (n-type) thick films were screen printed on PI substrates, respectively, followed by pressured sintering treatment. Firstly, $Bi_{0.5}Sb_{1.5}Te_3$ and $Bi_2Se_{0.3}Te_{2.7}$ ingots were individually hand-crushed into small particles using mortar and pestle. A two-step milling process was employed to grind the particles into fine powders of sub-micron to microns in size using a planetary ball miller (Retch, PM-100). The powders were mixed with stainless steel balls at a ratio of 1: 4 in weight. The first step was performed at 350 rpm for 30 min with large balls (diameter = 10 mm), while the second step was done with small balls (diameter = 2 mm) at 300 rpm for 3 h. A 10 min holding time was enforced every 20 min milling time to prevent excess heat accumulation and powder oxidation, if any, during the second milling process. Subsequently, we mixed the fine thermoelectric powders (7 g) with appropriate amount of organic binders (ethyl cellulose, 0.2g) and solvents (toluene 2.4g and ethanol 0.6g) for 2 h using a mixer to form the printing paste. A shadow mask was used to print Bi-Sb-Te and Bi-Se-Te stripes sequentially on a PI substrate

of 50 μm in thickness. Consequently, the printed stripes on the PI substrate were sandwiched in a metallic sample holder equipped with an embedded resistance heater. A pressure of 25 MPa was applied in the direction perpendicular to the specimen. The Bi-Sb-Te and Bi-Se-Te stripes were then cured under nitrogen ambient at elevated temperature by applying an electric current through the heater. During the sintering process, the temperature was ramped up to the set temperature in 30 min and maintained at the temperature for another 30 min. The post-sintered films are around 40 μm in thickness according to the cross-sectional scanning electron microscopy (SEM, SU-8010, Hitachi) inspection. The Seebeck coefficient, electrical resistivity (ρ) and carrier concentration (n) were measured by the temperature gradient approach [29], four-probe method and Hall effect measurement (HMS-3000, ECOPIA), respectively. The carrier mobility (μ) was determined according to the relation $\mu = 1/(\rho e n)$. To prepare a planar TEG, three pairs of Bi-Sb-Te and Bi-Se-Te thermoelements (20 mm × 3.4 mm × 0.04 mm) were consecutively printed on a PI substrate and cured at 345 °C under a pressure of 25 MPa. The contact electrodes between thermoelements were prepared by sputtering a Ni (300 nm)/Ag (700 nm) bilayer film on the patterned specimen through a shadow mask. Finally, the planar TEG was evaluated by putting two Cu blocks in contact to both ends of the thermoelements and measuring the electrical output performance. The temperature difference across the thermoelements was determined using an infrared thermographic recorder (VarioCAM HD580, JENOPTIK).

3. Results and discussion

3.1. Screen-printed thermoelectric films

Fig. 1 shows the cross-sectional SEM images of the Bi-Sb-Te and Bi-Se-Te films sintered at the temperature of 285, 315 and 345 °C for 30 min, respectively. A granular microstructure with tiny voids was observed in the films sintered at 285 °C, but not in the films sintered at the temperature above 300 °C. Note that the presence of pores may affect the transport properties of the sintered films. By raising the sintering temperature, we can eliminate the micropores in the Bi-Sb-Te and Bi-Se-Te films, as shown in Fig. 1. Moreover, some fracture facets were observed in the cross-sectional SEM image of the Bi-Se-Te film sintered at 345 °C (Fig. 1(f)). The facet morphology implies that the fracture mainly occurs along the van der Waals gap of the Bi-Te based compound rather than the grain boundary or powder interface [30]. It suggests that the Bi-Te powders in the screen-printed film were well sintered at 345 °C under a mechanical pressure of 25 MPa.

The microstructural change also reflects on the variation of transport properties of the sintered films. Both types of films reveal the decrease of electrical resistivity with increasing sintering temperature (Fig. 2(a,c)), which is mainly attributed to the greatly improved carrier mobility (Fig. 2(b,d)). Nevertheless, the Bi-Sb-Te and Bi-Se-Te films reveal an opposite trend in carrier concentration with sintering temperature (Fig. 2(b,d)). Note that the antisite defect, Sb_{Te}, has the lowest formation energy among various point defects in bismuth antimony telluride, which is responsible for the p-type conduction of Bi-Sb-Te thermoelements [31]. However, the raised sintering temperature would facilitate Te evaporation as well as formation of Sb-rich secondary phases at grain boundaries and surfaces in the p-type Bi-Sb-Te films [32]. The enhanced Sb-rich precipitation gives rise to the reduced Sb_{Te} defect density and the lower hole concentration in the p-type thermoelements. Alternatively, Se element that occupies the Te lattice site in the Bi-Se-Te thermoelement has an even higher vapor pressure than Te element. It is reasonably expected that there will be more vacancy
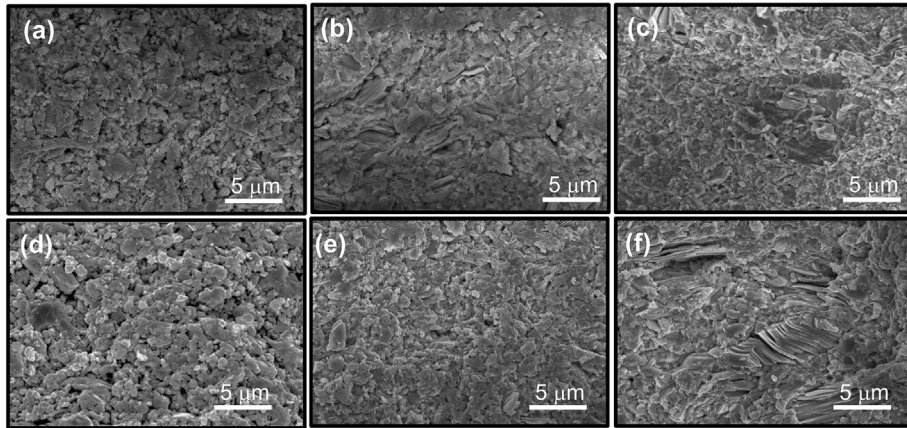
Fig. 1. Cross-sectional SEM images of (a)–(c) the Bi-Sb-Te films and (d)–(f) the Bi-Se-Te films sintered at the temperature of (a),(d) 285 °C; (b),(e) 315 °C; and(c),(f) 345 °C, respectively.
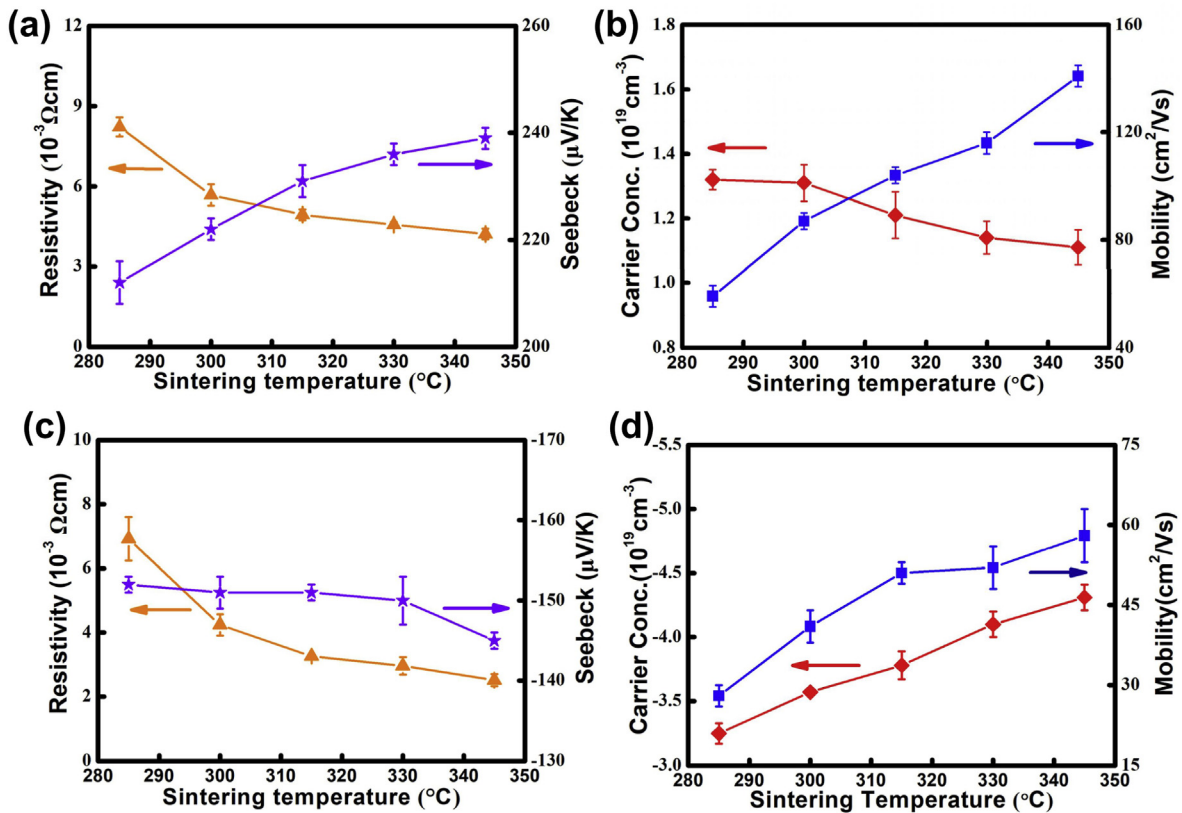

Fig. 2. Room-temperature transport properties of the (a),(b) Bi-Sb-Te films and (c),(d) Bi-Se-Te films sintered at 345 °C under a pressure of 25 MPa.

defects formed at the Te sites (V_{Te}) with the increase of sintering temperature. Since the V_{Te} acts as an electron donor, the electron concentration would increase with rising sintering temperature for the n-type thermoelements. The change of carrier concentration also reflects on the Seebeck coefficient according to the relation of $(8\pi^2 k_B^2/3eh^2)m^*T(\pi/3n)^{2/3}$, where n is the carrier concentration and m^* is the effective mass of charge carrier [33]. Generally, the Seebeck coefficient would decrease with increasing carrier concentration for the same material system. It explains why the Seebeck coefficient of the Bi-Sb-Te film increases, while that of Bi-Se-Te film decreases with sintering temperature (Fig. 2(a,c)).

A thermoelectric *PF* is commonly used to evaluate the output performance of thermoelectric materials [19,23]. Fig. 3 shows the room-temperature *PF* of the screen-printed Bi-Sb-Te and Bi-Se-Te films sintered at the temperature ranging from 285 °C to 345 °C. The *PF* values of both p- and n-type films increases monotonically with sintering temperature. The Bi-Sb-Te and Bi-Se-Te films show the largest *PF* values of 14.3 and 8.4 μW/cm·K², respective, after sintering at 345 °C. It is worth noting that the lower *PF* value for the Bi-Se-Te film is mainly attributed to the high V_{Te} concentration and small Seebeck coefficient. However, the *PF* values attained in this study have exceeded most of the screen-printed Bi-Te based films sintered at the temperature below 400 °C (p-type: 3.2−9.6 μW/cm·K²; n-type: 1.9−3.5 μW/cm·K²) [14,23,34,35]. The greatly
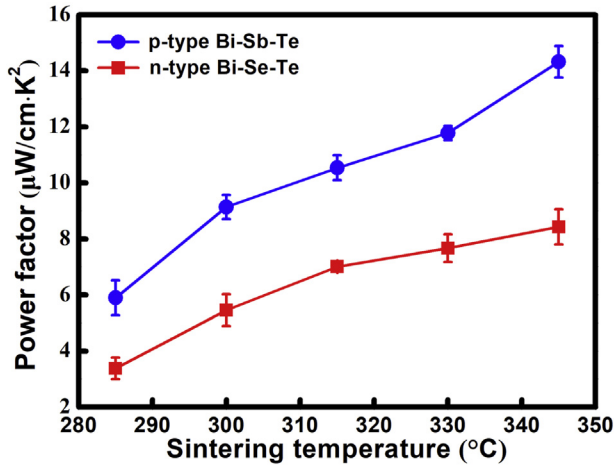
Fig. 3. The room-temperature thermoelectric power factors of the Bi-Sb-Te and Bi-Se-Te films sintered at different temperatures.

enhanced *PF* values are likely associated with controlled defect density and crystallographic texture in the Bi-Sb-Te and Bi-Se-Te thermoelements prepared by pressured sintering process, as reported in bulk Bi_2Te_3 systems [36,37]. Choi et al. have reported that the screen-printed $Bi_{0.5}Sb_{1.5}Te_3$ and $Bi_2Te_{2.7}Se_{0.3}$ thick films on the rigid Al_2O_3 substrate can achieve *PF* values of 25.7 and 16.6 μW/cm·K^2, respectively, after sintering at 500 °C [22]. However, the flexible PI substrate cannot sustain such a high temperature. By considering flexible TEG applications, the thermoelements implemented in the TEG devices studied were all sintered at the temperature of 345 °C.

3.2. Performance of flexible TEGs

A flexible planar TEG consisting of 3 pairs of thermoelements was fabricated by screen-printing and press-sintering processes. The interconnection between p- and n-type thermoelements were made by sputtering Ni/Ag bilayer electrode through a shadow mask. To measure the TEG output performance, two Cu blocks were attached to both sides of the thermoelements, serving as heat source and sink, respectively. The temperature profile of the thermoelement was measured by an infrared thermographic recorder, as show in Fig. 4. The output voltage and current were measured simultaneously as a function of ΔT ($= T_H - T_c$) under different load resistance (R_L). The internal resistance (R_{in}) of the TEG was extracted to be 26.3 Ω from the measured current and voltage at two different R_L according to the following relationship.
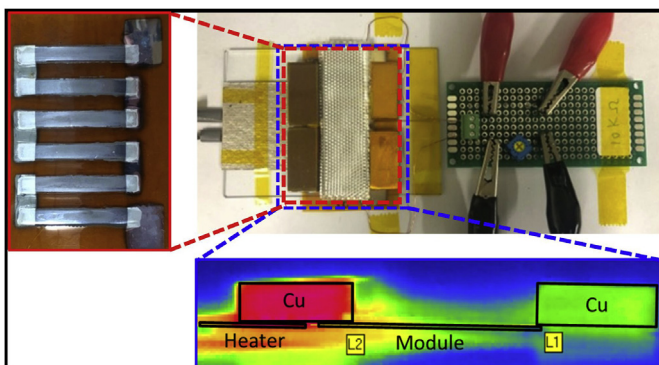

Fig. 4. Experimental setup for planar TEG performance evaluation.

$$R_{in} = (V_1 - V_2)/(I_2 - I_1) \tag{1}$$

The subscript 1 and 2 stand for the values measured with the load resistance R_{L1} and R_{L2}, respectively. It is worth mentioning that the overall electrical resistance of thermoelements is calculated to be 24.3 Ω based on the geometry and resistivity of the thermoelements. The discrepancy in electrical resistance (~2 Ω) is likely attributed to the metal electrode resistance and the metal/thermoelement contact resistance. By measuring the open-circuit voltage against ΔT, the three-paired TEG renders an open-circuit voltage of 1.2 mV per one degree of temperature difference across the thermoelements. Since the Seebeck coefficients of Bi-Sb-Te and Bi-Se-Te films are 240 μV/K and − 145 μV/K, respectively, the three-paired thermoelements would contribute 1.16 mV per one degree of temperature difference, which also agrees nicely with the measured value from the TEG.

The planar TEG performance was also evaluated under different R_L and ΔT conditions. Fig. 5(a) shows the hot side (T_{hot}) and cold side (T_{cold}) temperature against ΔT. The PI substrate provides good thermal isolation between heat source and sink so that T_{cold} is maintained at around 30 °C during the whole measurement. The output current, voltage and power of the TEG at different R_L and ΔT are shown in Fig. 5(b). Note that the intercept at the voltage axis represents the open-circuit voltage (V_{oc}). Fig. 5(c) depicts the TEG output power against R_L at different ΔT. The maximum output power (P_{max}) was obtained under the matched load condition. It is found that a maximum outpower of 50 μW was achieved when the TEG was operated at a temperature difference of 54.9 °C. Finally, the P_{max} and V_{oc} of the TEG are plotted against ΔT (Fig. 5(d)). Considering an ambient operation condition with $\Delta T < 10$ K, the planar TEG still can deliver a power of several μW, which is enough for many wearable microelectronic devices [38].

An intimidate contact to non-planar heat source and sink is the major advantage of the flexible TEG. However, the brittle nature of bismuth telluride-based materials makes the TEG less susceptible to the bending or folding configuration. Herein, a cyclic bending test was performed to examine the flexibility of the three-paired TEG. The TEG was forced to bend repeatedly in the longitudinal and transverse directions of thermoelements around a cylindrical steel rod of different radius of curvature (1, 1.5 and 2 cm). The electrical resistance of the TEG was measured right after certain bending cycles. Fig. 6 shows the variation of the TEG resistance normalized by the initial resistance (R_0) against the bending cycle at different bending radius and direction. It is noted that the three-paired TEG shows no significant electrical degradation after 1000 bending cycles except the longitudinal bending with a radius of curvature of 1 cm. (Fig. 6(a)). Moreover, the planar TEG is less vulnerable in the transverse bending condition due to less mechanical strain established in the spatially separated thermoelements (Fig. 6(b)).

Consider the longitudinal bending beam configuration (Fig. 7), the thermoelement is subjected to a tensile stress, while the PI substrate is under a compressive stress. There exists a neutral plane where the strain is equal to zero. The planar strain in the bilayer structure with a bending radius of R can be expressed as x/R, where x is radial position relative to the neutral plane. Based on the force balance in the bilayer structure, the average stress in the film layer can be formulated by

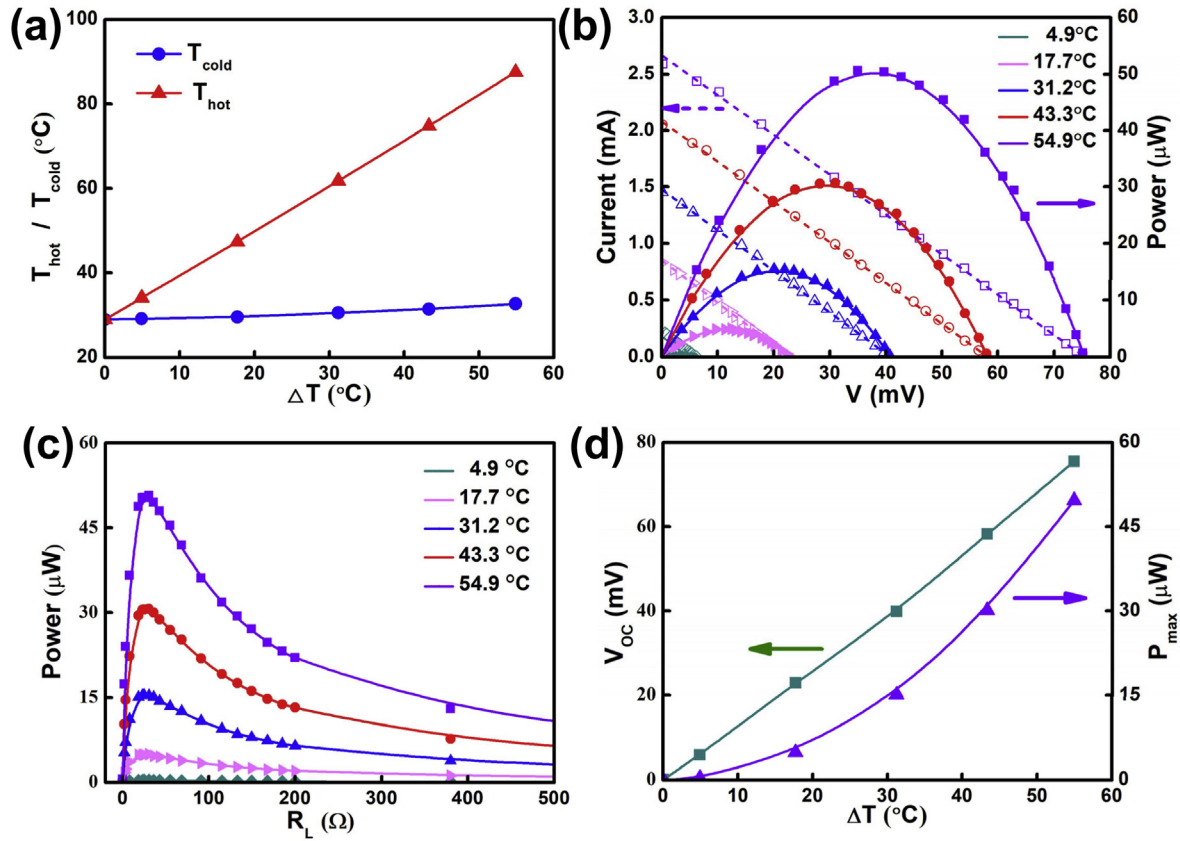$$\sigma_f = \left(1/t_f\right) \int_{x_0 - t_f}^{x_0} Y_f(x/R)dx \tag{2}$$

with

Fig. 5. Performance of the three-paired TEG under different load resistance (R_L) and temperature difference (ΔT). (a) Hot side (T_H) and cold side (T_C) temperature, (b) Electrical outputs under different ΔT, (c) Variation of output power with R_L under different ΔT, (d) Open-circuit voltage (V_{oc}) and maximum output power (P_{max}) under different ΔT.
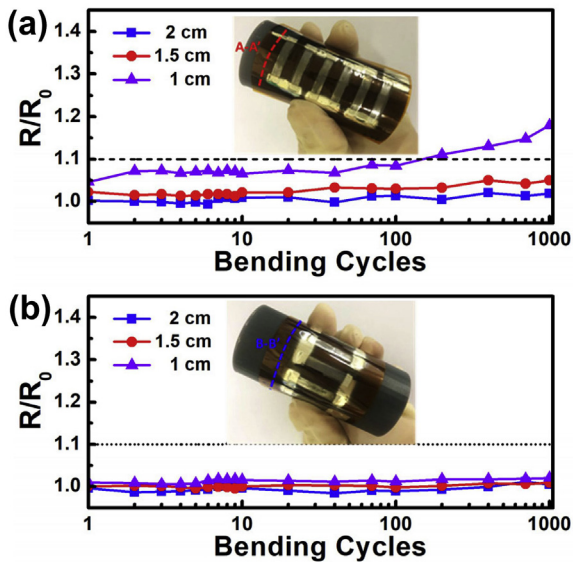

Fig. 6. Variation of normalized TEG resistance as a function of bending cycles under (a) longitudinal and (b) transverse bending with different bending radius of curvature.

Fig. 7. Strain distribution in the thermoelement/PI bilayer structure with the longitudinal bending configuration.

$$x_0 = \left(Y_f t_f^2 + Y_s t_s^2 + 2Y_s t_f t_s \right) \Big/ \left[2\left(Y_f t_f + Y_s t_s \right) \right]$$

where Y ($= E/(1 - \nu)$, E: Young's modulus, ν: Poisson's ratio) is biaxial modulus and t is layer thickness. The subscript f and s stand
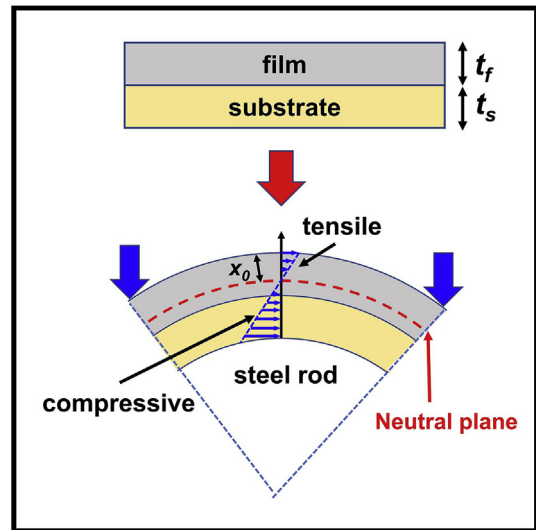
for thermoelectric film and substrate, respectively. Assuming the typical mechanical properties of Bi-Te based materials ($E = 45$ GPa, $\nu = 0.28$) [39] and PI ($E = 7.5$ GPa, $\nu = 0.35$) [40], the average tensile stresses in the thermoelement are calculated to be 38, 25 and 19 MPa when the bending radius is set to be 1, 1.5 and 2 cm, respectively. It has been reported that the mechanical strength of
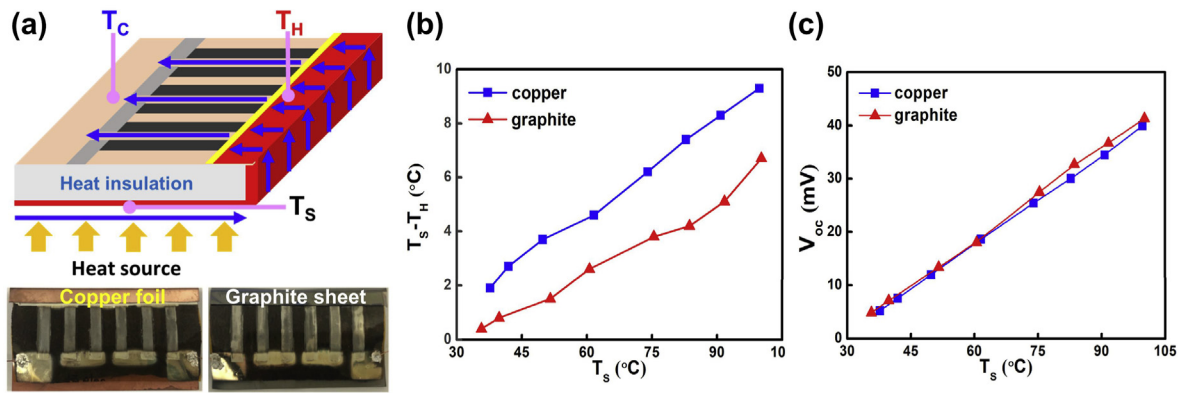
Fig. 8. (a) Heat collection design of a planar TEG, (b) Temperature drop ($T_S - T_H$) along different heat transmission layer, (c) Open-circuit voltage (V_{oc}) of TEG with copper and graphite HTL.

the Bi-Te based thermoelectric materials is in the magnitude of 30−40 MPa [39]. The thermoelements with a bending radius of 1 cm indeed are subjected to a tensile stress around the strength of Bi-Te based materials. It is reasonably expected that microcracks may form and propagate in the thermoelements with increasing bending cycles during the bending test. Actually, some cracks have been observed in the cross-sectional SEM image of the thermoelement after 1000 bending cycles at a radius of 1 cm, supporting the increase of electrical resistance of the TEG with bending cycles.

The planar TEG owns higher output voltage than the vertical TEG because a large ΔT can be established across the thermoelements. However, a large device footprint would lead to a lowered power density for the planar TEG. Besides, the planar TEG requires the heat sink and source located at the same side of the device. An appropriate heat collection and thermal isolation design is needed for the best usage of planar heat source. Herein, a heat transmission layer (HTL) made of Cu foil or graphite sheet was attached to one end of thermoelements using thermally conductive tape and folded to the back side of the planar TEG, as shown in Fig. 8(a). An insulating foam layer was inserted in between the TEG and the HTL to prevent heat dissipation in the out-of-plane direction. Three thermocouples were used to measure the temperatures at the heat source (T_S), hot side (T_H) and cold side (T_C) of the TEG device. The proposed configuration can make full usage of the device footprint for heat collection by lowering the TEG/heat source thermal contact resistance. Fig. 8(b) shows the temperature drop between heat source and hot-side temperature ($T_S - T_H$) as a function of T_S for the planar TEG with Cu and graphite HTL, respectively. It is found that the graphite HTL exhibits a better heat conduction capability, i.e. smaller temperature drop ($T_S - T_H$), than the Cu HTL for the planar TEG studied. Thus, the TEG with graphite HTL provides a slightly higher output voltage (Fig. 8(c)). By adapting this design, the planar TEG can attain a maximum output power density of 58.3 μW/cm^2 under a ΔT of 5.7 °C with a graphite HTL attached to a heat source at the temperature of 39.8 °C. It means that the TEG can supply a micro-watt scale electricity with a constant low-temperature heat source such as human body, which can be applied in many wearable microelectronics or wireless sensing/transmission devices.

4. Conclusions

In this study we fabricated a three-paired planar TEG on a flexible substrate by using screen printing and pressured sintering techniques. The planar TEG demonstrated an outpower of 50 μW at a temperature difference of 54.9 °C. The TEG shows good flexibility and no electrical degradation after 1000 cycles of bending along the

longitudinal and transverse directions of the thermoelements. A directional heat collection configuration is also proposed to improve the TEG performance by combining an HTL and thermal isolation foam with the planar TEG.

Declaration of competing interest

The authors declare that they have no known competing financial interests or personal relationships that could have appeared to influence the work reported in this paper.

CRediT authorship contribution statement

Pin-Shiuan Chang: Data curation, Formal analysis, Methodology. **Chien-Neng Liao:** Data curation, Formal analysis, Writing - original draft, Supervision.

Acknowledgement

References

[1] L.E. Bell, Cooling, heating, generating power, and recovering waste heat with thermoelectric systems, Science 321 (2008) 1457−1461.
[2] Y. Sadia, Z. Aminov, D. Mogilyansky, Y. Gelbstein, Texture anisotropy of higher manganese silicide following arc-melting and hot-pressing, Intermetallics 68 (2016) 71−77.
[3] I. Cohen, M. Kaller, G. Komisarchik, D. Fuks, Y. Gelbstein, Enhancement of the thermoelectric properties of n-type PbTe by Na and Cl co-doping, J. Mater. Chem. C 3 (2015) 9559−9564.
[4] G. Komisarchik, D. Fuks, Y. Gelbstein, High thermoelectric potential of n-type Pb$_{1-x}$Ti$_x$Te alloys, J. Appl. Phys. 120 (2016), 055104.
[5] Gilad M. Guttmann, David Dadon, Yaniv Gelbstein, Electronic tuning of the transport properties of off-stoichiometric Pb$_x$Sn$_{1-x}$Te thermoelectric alloys by Bi$_2$Te$_3$ doping, J. Appl. Phys. 118 (2015), 065102.
[6] O. Appel, Y. Gelbstein, A comparison between the effects of Sb and Bi doping on the thermoelectric properties of the Ti$_{0.3}$Zr$_{0.35}$Hf$_{0.35}$NiSn half-heusler alloy, J. Electron. Mater. 43 (2014) 1976−1982.
[7] F.P. Zhang, Q.M. Lu, X. Zhang, J.X. Zhang, First principle investigation of electronic structure of CaMnO$_3$ thermoelectric, J. Alloys Compd. 509 (2011) 542−545.
[8] F.P. Zhang, Q.M. Lu, X. Zhang, J.X. Zhang, Electrical transport properties of CaMnO$_3$ thermoelectric compound: a theoretical study, J. Phys. Chem. Solid. 74 (2013) 1859−1864.
[9] M. Strasser, R. Aigner, C. Lauterbach, T. Sturm, M. Franosch, G. Wachutka,

Micromachined CMOS thermoelectric generators as on-chip power supply, Sensor Actuat. A Phys. 114 (2004) 362−370.

[10] K.V. Selvan, M.N. Hasan, M.S. Mohamed Ali, Methodological reviews and analyses on the emerging research trends and progresses of thermoelectric generators, Int. J. Energy Res. 43 (2019) 113−140.

[11] W. Glatz, E. Schwyter, L. Durrer, C. Hierold, Bi₂Te₃-based flexible micro thermoelectric generator with optimized design, J. Microelectromech. Syst. 18 (2009) 763−772.

[12] I. Chowdhury, R. Prasher, K. Lofgreen, G. Chrysler, S. Narasimhan, R. Mahajan, D. Koester, R. Alley, R. Venkatasubramanian, On-chip cooling by superlattice-based thin-film thermoelectrics, Nat. Nanotechnol. 4 (2009) 235.

[13] Z. Yuan, X. Tang, Y. Liu, Z. Xu, K. Liu, J. Li, Z. Zhang, H. Wang, Improving the performance of a screen-printed micro-radioisotope thermoelectric generator through stacking integration, J. Power Sources 414 (2019) 509−516.

[14] Z. Yuan, X. Tang, Y. Liu, Z. Xu, K. Liu, Z. Zhang, W. Chen, J. Li, A stacked and miniaturized radioisotope thermoelectric generator by screen printing, Sensor. Actuator. A 267 (2017) 496−504.

[15] Y.J. Kim, S.J. Kim, H. Choi, C.S. Kim, G. Lee, S.H. Park, B.J. Cho, Realization of high-performance screen-printed flexible thermoelectric generator by improving contact characteristics, Adv. Mater. Interfaces 4 (2017) 1700870.

[16] H. Choi, Y.J. Kim, C.S. Kim, H.M. Yang, M.-W. Oh, B.J. Cho, Enhancement of reproducibility and reliability in a high-performance flexible thermoelectric generator using screen-printed materials, Nano Energy 46 (2018) 39−44.

[17] J.P. Rojas, D. Conchouso, A. Arevalo, D. Singh, I.G. Foulds, M.M. Hussain, Paper-based origami flexible and foldable thermoelectric nanogenerator, Nano Energy 31 (2017) 296−301.

[18] Y. Zhou, L. Li, Q. Tan, J.-F. Li, Thermoelectric properties of Pb-doped bismuth telluride thin films deposited by magnetron sputtering, J. Alloys Compd. 590 (2014) 362−367.

[19] K. Takayama, M. Takashiri, Multi-layered-stack thermoelectric generators using p-type Sb₂Te₃ and n-type Bi₂Te₃ thin films by radio-frequency magnetron sputtering, Vacuum 144 (2017) 164−171.

[20] S.H. Lee, H. Shen, S. Han, Flexible thermoelectric module using Bi-Te and Sb-Te thin films for temperature sensors, J. Electron. Mater. 48 (2019) 5464−5470.

[21] S.-D. Kwon, B.-k. Ju, S.-J. Yoon, J.-S. Kim, Fabrication of bismuth telluride-based alloy thin film thermoelectric devices grown by metal organic chemical vapor deposition, J. Electron. Mater. 38 (2009) 920−924.

[22] H. Choi, S.J. Kim, Y. Kim, J.H. We, M.-W. Oh, B.J. Cho, Enhanced thermoelectric properties of screen-printed Bi₀.₅Sb₁.₅Te₃ and Bi₂Te₂.₇Se₀.₃ thick films using a post annealing process with mechanical pressure, J. Mater. Chem. C 5 (2017) 8559−8565.

[23] W. Hou, X. Nie, W. Zhao, H. Zhou, X. Mu, W. Zhu, Q. Zhang, Fabrication and excellent performances of Bi₀.₅Sb₁.₅Te₃/epoxy flexible thermoelectric cooling devices, Nano Energy 50 (2018) 766−776.

[24] T. Varghese, C. Dun, N. Kempf, M. Saeidi-Javash, C. Karthik, J. Richardson, C. Hollar, D. Estrada, Y. Zhang, Flexible thermoelectric devices of ultrahigh power factor by scalable printing and interface engineering, Adv. Funct. Mater. 30 (2020) 1905796.

[25] S. Xu, M. Hong, X.-L. Shi, Y. Wang, L. Ge, Y. Bai, L. Wang, M. Dargusch, J. Zou, Z.-G. Chen, High-performance PEDOT:PSS flexible thermoelectric materials and their devices by triple post-treatments, Chem. Mater. 31 (2019) 5238−5244.

[26] Y. Wang, L. Yang, X.-L. Shi, X. Shi, L. Chen, M.S. Dargusch, J. Zou, Z.-G. Chen, Flexible thermoelectric materials and generators: challenges and innovations, Adv. Mater. 31 (2019) 1807916.

[27] S. Jo, S. Choo, F. Kim, S.H. Heo, J.S. Son, Ink processing for thermoelectric materials and power-generating devices, Adv. Mater. 31 (2019) 1804930.

[28] M.S. Hossain, T. Li, Y. Yu, J. Yong, J.-H. Bahk, E. Skafidas, Recent advances in printable thermoelectric devices: materials, printing techniques, and applications, RSC Adv. 10 (2020) 8421−8434.

[29] C.-N. Liao, T.-H. She, P.-J. Liao, H.-S. Chu, Oscillatory transport properties of thermally annealed Bi/Te multilayer thin films, J. Electrochem. Soc. 154 (2007) H304−H308.

[30] G. Wang, T. Cagin, Electronic structure of the thermoelectric materials Bi₂Te₃ and Sb₂Te₃ from first-principles calculations, Phys. Rev. B 76 (2007), 075201.

[31] J. Horak, K. Čermák, L. Koudelka, Energy formation of antisite defects in doped Sb₂Te₃ and Bi₂Te₃ crystals, J. Phys. Chem. Solid. 47 (1986) 805−809.

[32] J. Navratil, Z. Starý, T. Plechacek, Thermoelectric properties of p-type antimony bismuth telluride alloys prepared by cold pressing, Mater. Res. Bull. 31 (1996) 1559−1566.

[33] G.J. Snyder, E.S. Toberer, Complex thermoelectric materials, Nat. Mater. 7 (2008) 105−114.

[34] Y.S. Jung, D.H. Jeong, S.B. Kang, F. Kim, M.H. Jeong, K.-S. Lee, J.S. Son, J.M. Baik, J.-S. Kim, K.J. Choi, Wearable solar thermoelectric generator driven by unprecedentedly high temperature difference, Nano energy 40 (2017) 663−672.

[35] K. Kato, K. Kuriyama, T. Yabuki, K. Miyazaki, Organic-inorganic thermoelectric material for a printed generator, J. Phys. Conf. Ser 1052 (2018), 012008.

[36] Y. Wang, W.-D. Liu, X.-L. Shi, M. Hong, L.-J. Wang, M. Li, H. Wang, J. Zou, Z.-G. Chen, Enhanced thermoelectric properties of nanostructured n-type Bi2Te3 by suppressing Te vacancy through non-equilibrium fast reaction, Chem. Eng. J. (2019), https://doi.org/10.1016/j.cej.2019.123513 (in press).

[37] D. Bao, J. Chen, Y. Yu, W. Liu, L. Huang, G. Han, J. Tang, D. Zhou, L. Yang, Z.-G. Chen, Texture-dependent thermoelectric properties of nano-structured Bi₂Te₃, Chem. Eng. J. 388 (2020) 124295.

[38] A.R.M. Siddique, S. Mahmud, B. Van Heyst, A review of the state of the science on wearable thermoelectric power generators (TEGs) and their existing challenges, Renew. Sustain. Energy Rev. 73 (2017) 730−744.

[39] M. Picard, S. Turenne, D. Vasilevskiy, R. Masut, Numerical simulation of performance and thermomechanical behavior of thermoelectric modules with segmented bismuth-telluride-based legs, J. Electron. Mater. 42 (2013) 2343−2349.

[40] J. Dolbow, M. Gosz, Effect of out-of-plane properties of a polyimide film on the stress fields in microelectronic structures, Mech. Mater. 23 (1996) 311−321.